Inorganic Chemistry

ARTICLE

pubs.acs.org/IC

P123-PMMA Dual-Templating Generation and Unique Physicochemical Properties of Three-Dimensionally Ordered Macroporous Iron Oxides with Nanovoids in the Crystalline Walls

Ruzhen Zhang,[†] Hongxing Dai,[*,†] Yucheng Du,[‡] Lei Zhang,[†] Jiguang Deng,[†] Yunsheng Xia,[†] Zhenxuan Zhao,[†] Xue Meng,[†] and Yuxi Liu[†]

[†]Laboratory of Catalysis Chemistry and Nanoscience, Department of Chemistry and Chemical Engineering, College of Environmental and Energy Engineering, and [‡]Key Lab of Advanced Functional Materials, Ministry of Education, College of Materials Science and Engineering, Beijing University of Technology, Beijing 100124, China

Supporting Information

ABSTRACT: Three-dimensionally (3D) ordered macroporous (3DOM) iron oxides with nanovoids in the rhombohedrally crystallized macroporous walls were fabricated by adopting the dual-templating [Pluronic P123 and poly(methyl methacrylate) (PMMA) colloidal microspheres] strategy with ferric nitrate as the metal precursor in an ethanol or ethylene glycol and methanol mixed solution and after calcination at 550 °C. The possible formation mechanisms of such architectured materials were discussed. The physicochemical properties of the materials were characterized by means of techniques such as XRD, TGA/DSC, FT-IR, BET, HRSEM, HRTEM/SAED, UV−vis, XPS, and H_2-TPR. The catalytic properties of the materials were also examined using toluene oxidation as a probe reaction. It is shown that 3DOM-structured α-Fe_2O_3 without nanovoids in the macroporous walls was formed in the absence of P123 during the fabrication process, whereas the dual-templating strategy gave rise to α-Fe_2O_3 materials that possessed high-quality 3DOM structures with the presence of nanovoids in the polycrystalline macropore walls and higher surface areas (32−46 m^2/g). The surfactant P123 played a key role in the generation of nanovoids within the walls of the 3DOM-architectured iron oxides. There was the presence of multivalent iron ions and adsorbed oxygen species on the surface of each sample, with the trivalent iron ion and oxygen adspecies concentrations being different from sample to sample. The dual-templating fabricated iron oxide samples exhibited much better low-temperature reducibility than the bulk counterpart. The copresence of a 3DOM-structured skeleton and nanovoids in the macropore walls gave rise to a drop in the band-gap energy of iron oxide. The higher oxygen adspecies amounts, larger surface areas, better low-temperature reducibility, and unique nanovoid-containing 3DOM structures of the iron oxide materials accounted for their excellent catalytic performance in the oxidation of toluene.

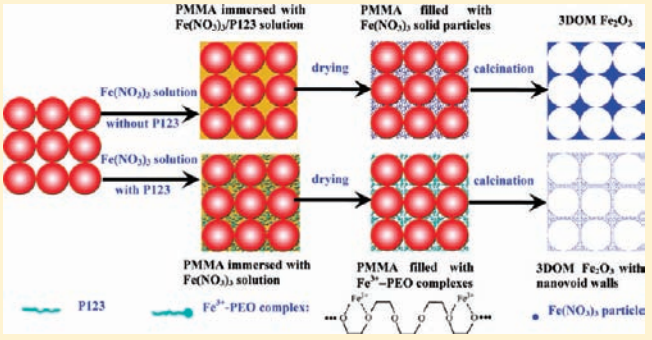

INTRODUCTION

Porous transition-metal oxide materials have important roles to play in physical and chemical fields, such as electronics, magnetism, adsorption, and heterogeneous catalysis. Such materials possess high surface areas, large pore volumes, and regular pore structures, and these unique features make them attractive for the design of novel catalytic materials with high performance.[1] The transition-metal oxides with three-dimensionally (3D) ordered and wormhole-like mesoporous architectures have received particular attention because of their potential utilization as a catalyst or support for a large number of redox-involving reactions. Generally speaking, the fabrication of transition-metal oxides with mesoporous nanostructures requires two kinds of structure-directing agents: one is a surfactant or block copolymer, called a "soft template"; the other is a mesoporous carbon and silica or polymer microsphere, called a "hard template".

In the past decade, many authors reported the soft-templating synthesis of mesoporous iron oxides. For example, Perkas et al. synthesized a mesoporous iron−titanium oxide composite by the ultrasound-assisted method with dodecylamine as the soft template and iron(III) ethoxide and titanium(IV) isopropoxide as metal precursors.[2] Song et al. developed a versatile, low-cost, and environmentally friendly strategy to produce mesoporous Mn_2O_3, Fe_2O_3, Co_3O_4, NiO, CuO, and ZnO with various morphologies via a hydrothermal pathway with cetyltrimethylammonium bromide (CTAB) as the soft template and inorganic metal nitrates as the precursors.[3] Gedanken and co-workers

Received: November 26, 2010
Published: February 16, 2011

synthesized mesoporous iron oxides using a sonochemical technique with iron(III) ethoxide as the inorganic precursor and CTAB as the organic structure-directing agent.[4] Wan et al. generated transparent and uniform nanocrystalline α-Fe_2O_3 thin films with wormlike morphology by the evaporation-induced self-assembly (EISA) method with triblock copolymer F127 ($EO_{106}PO_{70}EO_{106}$) as the template and ferric nitrate as the inorganic source.[5] Via the EISA process with a novel block copolymer [poly(isobutylene)-*block*-poly(ethylene oxide) or poly(ethylene-*co*-butylene)-*b*-poly(ethylene oxide)] as the template, Smarsly and co-workers fabricated crack-free mesoporous α-Fe_2O_3 thin films.[6] Using the sonication method with sodium dodecyl sulfate as the surfactant and ferric nitrate as the metal source, Gedanken and co-workers generated straight-extended layered mesostructured iron oxide materials.[7]

With the establishment of hard-templating synthesis techniques, ordered porous iron oxides can be produced. For example, Shi et al. employed continuous thin films of 3D-ordered mesoporous silica SBA-16 as the template to synthesize 3D porous iron oxide crystals by electrochemical deposition of iron metal and subsequent in situ oxidation.[8] Bruce and co-workers fabricated α-Fe_2O_3 materials with ordered and disordered mesoporous walls using the 3D-ordered mesoporous silica KIT-6 as the hard template and ferric nitrate as the precursor;[9] the same group also reported the successful synthesis of two-dimensionally (2D) ordered hexagonal mesoporous iron oxide and 3D cubic mesoporous iron oxide with microporous walls by adopting decylamine as the template and iron(III) ethoxide as the precursor and without calcination.[10] Kang et al. employed highly ordered mesoporous carbon (CMK-3, which was derived from the nanocasting of 2D-ordered mesoporous silica SBA-15) as the hard template via the nanoreplication technique to fabricate mesoporous V_2O_5, MoO_3, WO_3, MnO_2, and Fe_2O_3.[11] Kong et al. also utilized mesoporous carbon CMK-3 as the hard template to obtain crystalline wormhole-like mesoporous Fe_2O_3.[12] In addition to the above synthesis methods, there are also alternatives for the generation of porous iron oxides. For instance, Zhao and co-workers fabricated mesoporous Fe_2O_3 microspheres by the polymerization of (urea and formaldehyde)-induced ferric hydroxide colloid aggregation.[13] Lezau et al. obtained wormhole-like mesoporous iron oxide using a ligand-assisted templating method with a trischelating triol (i.e., 1,1,1-trishydroxymethylundecane) as the surfactant and iron(III) ethoxide as the metal source.[14] Yu et al. fabricated mesoporous Fe_2O_3 via a solution route with dioctylsulfosuccinate, oxalic acid, and iron sulfate as starting materials.[15] Zhou et al. synthesized wormhole-like mesoporous Fe_3O_4 with a pore size range of 8−14 nm via a coprecipitation process with yeast cells as the template.[16]

Compared to the bulk transition-metal oxides, the 3D-ordered macroporous (3DOM)-structured counterparts display unique physicochemical properties because of their interconnected porous structures, higher surface areas, strong redox ability, and good catalytic performance. Such features make these materials useful in photonic crystals, catalysis, electrochemistry, and separation.[17] The most commonly employed strategy to generate 3DOM metal oxides involves an alkoxide-based sol−gel process, in which a colloidal crystal [e.g., well-arrayed monodispersed microspheres of polystyrene, poly(methyl methacrylate) (PMMA), silica, or carbon] is used as the hard template and liquid metal alkoxides, nitrates, or acetates are used as the metal precursor. The as-obtained interconnected porous materials with high porosity facilitate the transport of guest molecules and particles in potential catalysis and filtration.[18] By using an ethylene glycol−methanol (EG−MeOH) mixed solution of metal nitrates, Ueda and co-workers fabricated 3DOM single-metal oxides (Al_2O_3, Fe_2O_3, and Mn_2O_3)[18d] and mixed-metal oxides [$La_{1-x}Sr_xFeO_3$, MFe_2O_4 (M = Zn, Ni, Co), $ZnAl_2O_4$, $ZnCr_2O_4$, $LaAlO_3$, and $LaMnO_3$].[18] Although 3DOM metal oxides can be synthesized according to the above strategy, their surface areas are still relatively low (13−35 m^2/g) especially after calcination at high temperatures (>500 °C) and, furthermore, there was no formation of mesopores or nanometered voids (called nanovoids, which do not go through from the top surface to the bottom surface) in the walls of the macropores. These drawbacks inhibit wide applications of such architectured materials. Therefore, it is highly desired to develop an effective strategy for the fabrication of high-surface-area 3DOM metal oxides with the presence of mesopores or nanovoids in the crystalline walls. Although silica with a bimodal distribution of meso- and macropores[19] or micro- and macropores[20] can be fabricated, metal oxides with hierarchically mesoporous/nanovoid and macroporous structures are rarely reported in the literature.

In the past several years, we have investigated the synthesis and physicochemical properties of nano/microsized perovskite [e.g., $La_{1-x}Sr_xMO_3$ (M = Mn, Co, Fe) and $LaCoO_3$/SBA-15][21] materials and monoclinic $BiVO_4$,[22] mesoporous MgO[23] and CaO,[24] and 3DOM-structured MgO (with wormhole-like mesoporous walls), γ-Al_2O_3 (with 3D-ordered mesoporous walls), and $Ce_{1-x}Zr_xO_2$ (with wormhole-like mesoporous walls).[25] These perovskite materials showed excellent performance for the catalytic removal of volatile organic compounds (e.g., toluene and ethyl acetate). Recently, we have extended our attention to the fabrication and catalysis chemistry of mesoporous transition-metal oxides.[26] In this work, we report the controlled generation and physicochemical property characterization of nanovoid-containing 3DOM iron oxides by using the dual-templating (surfactant P123 and colloidal PMMA microspheres) strategy with iron nitrate as the metal source in an absolute ethanol (EtOH) or EG and MeOH mixed solution.

EXPERIMENTAL SECTION

Sample Generation. The well-arrayed hard-template PMMA microspheres with an average diameter of ca. 300 nm (Figure S1 of the Supporting Information) were synthesized according to the procedures described elsewhere.[2,25] The macroporous Fe_2O_3 samples with nanovoids in the crystalline walls were fabricated using the dual-templating strategy. In a typical synthesis, 10 mmol of $Fe(NO_3)_3 \cdot 9H_2O$ and 0.50, 1.00, 4.00, or 8.00 g of P123 (M_{av} = 5800) were dissolved in 10 mL of absolute EtOH or in 10 mL of an anhydrous EG and MeOH mixed solution (EG/MeOH volumetric ratio = 3/2) under ultrasonic radiation (90 Hz), in which the iron nitrate concentration of the resulting solution was 1 mol/L and the molar ratio of Fe/P123 was 116, 232, 928, and 1856, respectively. A total of 2.00 g of highly ordered PMMA microspheres was added and soaked by the above mixed solution. After the PMMA microspheres were thoroughly wetted, the excessive liquid was filtered via a Buchner funnel connected to a vacuum (0.07 MPa). The obtained intermediate was dried in a desiccator using anhydrous calcium chloride as the desiccating agent (relative humidity <50%) at room temperature (RT) for 12 h (in the P123-free case) or 24 h (in the P123-added case), calcined in air at a ramp of 1 °C/min from RT to 300 °C, kept at this temperature for 3 h, then increased to 550 or

dx.doi.org/10.1021/ic1023604 |*Inorg. Chem.* 2011, 50, 2534–2544

Table 1. Fabrication Parameters, BET Surface Areas, Band-Gap Energies, Surface Compositions, and H_2 Consumption of the As-Fabricated Fe_2O_3 Samples

sample	hard/soft template	Fe/soft template molar ratio	solvent	calcination conditions	surface area (m^2/g)	band-gap energy (eV)	Fe^{3+}/Fe^{2+} molar ratio	O_{ads}/O_{latt} molar ratio	H_2 consumption (mmol/g) 190−350 °C	H_2 consumption (mmol/g) 350−700 °C
Fe_2O_3−*bulk*				650 °C, 3 h	7.0	2.10	3.59	0.74	1.05	16.1
Fe_2O_3−1	PMMA/−		EtOH	(300 °C, 3 h) → (550 °C, 3 h)	16.3	2.08	2.97	0.87	1.92	13.4
Fe_2O_3−2	PMMA/P123	116	EtOH	(300 °C, 3 h) → (550 °C, 3 h)	42.4	1.95	2.95	1.53	2.09	13.4
Fe_2O_3−3	PMMA/P123	232	EtOH	(300 °C, 3 h) → (550 °C, 3 h)	46.1	1.92	2.82	1.63	2.19	13.3
Fe_2O_3−4	PMMA/P123	232	EtOH	(300 °C, 3 h) → (650 °C, 3 h)	16.9	2.06	3.61	0.83	1.85	13.7
Fe_2O_3−5	PMMA/P123	928	EtOH	(300 °C, 3 h) → (550 °C, 3 h)	35.2	1.98	3.08	1.25	2.01	12.8
Fe_2O_3−6	PMMA/P123	1856	EtOH	(300 °C, 3 h) → (550 °C, 3 h)	45.1	1.95	2.80	1.04	2.21	13.4
Fe_2O_3−7	PMMA/P123	232	EG-MeOH [a]	(300 °C, 3 h) → (550 °C, 3 h)	32.2	2.03	2.75	1.21	2.46	13.1

[a] 10 mL of an EG and MeOH mixture with EG/MeOH volumetric ratio = 3/2.

650 °C at the same heating rate, and maintained at this temperature for 3 h, thus obtaining the porous iron oxide products. For the sake of a better presentation, we denoted these samples as Fe_2O_3−x (x = 1−7), as described in Table 1. For comparison purposes, we also prepared a nonporous iron oxide sample (denoted as Fe_2O_3−*bulk*) by calcining a certain amount of ferric nitrate in air at 650 °C for 3 h.

All of the chemicals (analytical reagent grade purity) were purchased from Beijing Chemicals Company and used without further purification.

Physicochemical Property Characterization. All of the as-fabricated samples were characterized by means of techniques such as X-ray diffraction (XRD), thermogravimetric analysis (TGA), and differential scanning calorimetry (DSC), Fourier transform infrared (FT-IR) spectroscopy, high-resolution scanning electron microscopy (HRSEM), high-resolution transmission electron microscopy (HRTEM), selected-area electron diffraction (SAED), N_2 adsorption−desorption (Brunauer−Emmett−Teller, BET), ultraviolet−visible (UV−vis) diffuse-reflectance spectroscopy, X-ray photoelectron spectroscopy (XPS), and H_2 temperature-programmed reduction (H_2-TPR). The catalytic performance of the materials was evaluated for the oxidation of toluene. The detailed procedures are described in the Supporting Information.

RESULTS AND DISCUSSION

Crystal Structure. Figure 1 shows the XRD patterns of the as-fabricated iron oxide samples. By comparing the XRD pattern of the standard Fe_2O_3 sample (JCPDS no. 87-1164), one can deduce that the eight iron oxide samples were α-Fe_2O_3 with a rhombohedral crystal structure.[27] All of the Bragg diffraction peaks in the 2θ range of 10−80° can be well indexed, as indicated in Figure 1h. The results suggest that calcination at a temperature of above 550 °C could guarantee the complete decomposition of iron nitrate to α-Fe_2O_3. All of the α-Fe_2O_3 samples showed a slight difference in the intensity of the XRD signals, indicating that the addition of P123 exerted a minor

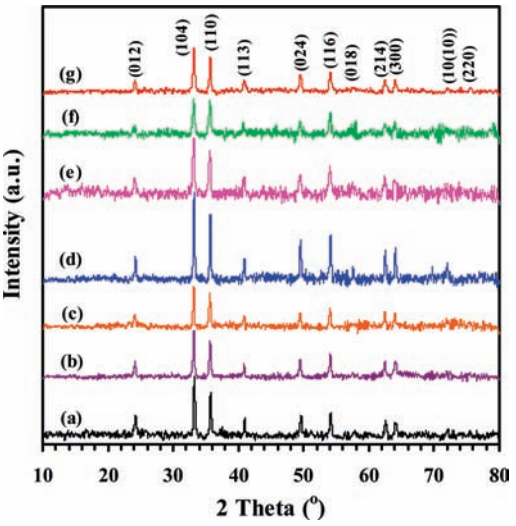

Figure 1. XRD patterns of (a) Fe_2O_3−1, (b) Fe_2O_3−2, (c) Fe_2O_3−3, (d) Fe_2O_3−4, (e) Fe_2O_3−5, (f) Fe_2O_3−6, and (g) Fe_2O_3−7.

influence on the crystallinity. A rise in the calcination temperature from 550 to 650 °C led to improvement in the crystallinity of α-Fe_2O_3.

Figure 2 illustrates the TGA/DSC profiles of the typical iron oxide samples before calcination (i.e., the uncalcined Fe_2O_3−1 and Fe_2O_3−3 samples prepared without or with the assistance of P123, respectively). It is observed from Figure 2A that there were weight losses of ca. 8, 25, and 64 wt % in the temperature ranges of 30−86, 86−254, and 254−400 °C, accompanied by the appearance of well-resolved endothermic signals centered at 38, 117, and 372 °C, respectively. The three weight losses could be attributed to the successive removal of adsorbed water or EtOH, decomposition of $Fe(NO_3)_3$,[28] and oxidation of PMMA.[18d,25] From Figure 2B, one can see three weight losses

dx.doi.org/10.1021/ic1023604 |*Inorg. Chem.* 2011, 50, 2534–2544

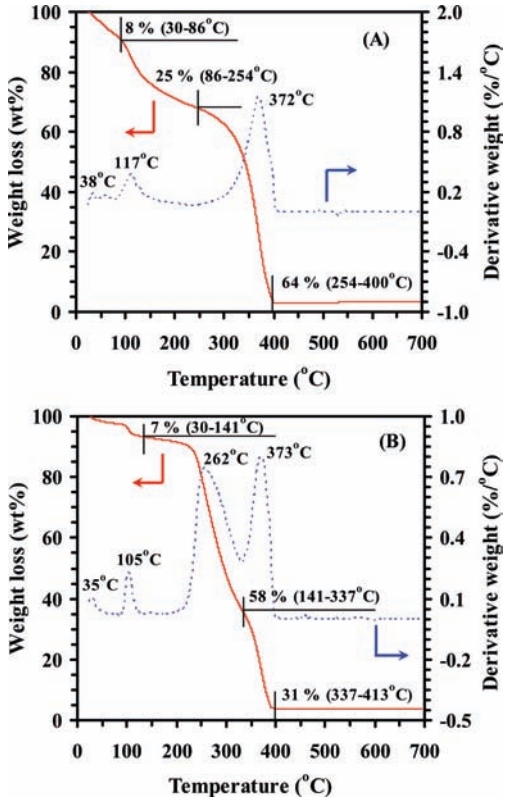

Figure 2. TGA/DSC profiles of (A) uncalcined Fe_2O_3−1 and (B) uncalcined Fe_2O_3−3.

in the temperature ranges of 30−141, 141−337, and 337−413 °C, where the respective weight losses were ca. 7, 58, and 31 wt %, accompanied by the recording of endothermic signals centered at 105, 262, and 373 °C, respectively. These weight losses could be reasonably assigned to the elimination of adsorbed water or EtOH, decomposition of $Fe(NO_3)_3$,[28] and oxidation of P123 and PMMA,[18d,25] accordingly. These results clearly demonstrate that calcination of the sample intermediates above 413 °C was appropriate to generate α-Fe_2O_3 crystals. In addition, the FT-IR results shown in Figure S2 in the Supporting Information further confirm that the surfactant P123 and hard-template PMMA could be completely removed after calcination at 550 °C.

Pore Structure and Surface Area. Figure 3 shows the HRSEM images of the as-fabricated Fe_2O_3−x samples. It is clearly observed that there were a number of 3D-ordered macroporous entities (pore size = 180−200 nm) in the Fe_2O_3−1 sample derived in the absence of surfactant P123 (Figure 3a,b), which exhibited similar pore structures of Fe_2O_3 obtained by other researchers.[18d] With the addition of P123, ordered macroporous architectures were also generated in the other six Fe_2O_3 samples and their macropore qualities were different upon variation in the fabrication conditions (Figure 3c−l). For the Fe_2O_3−2 sample, a number of 3DOM-organized entities (Figure 3c,d) with macropore sizes of 160−200 nm were formed. A rise in the P123 concentration from Fe/P123 molar ratio = 116 to 232 led to generation of a 3DOM structure with interconnected pore walls (Figure 3e,f). Raising the calcination temperature from 550 to 650 °C resulted in a change in the pore-wall structure (Figure 3g) of the Fe_2O_3−4 sample, although the 3DOM array was retained. A further rise in the P123 concentration from Fe/P123 molar ratio = 232 to 928 or 1856 gave rise to the Fe_2O_3−5 and Fe_2O_3−6 samples, which also displayed 3DOM structure (Figure 3h−j), but their 3DOM quality became worse compared to that of the Fe_2O_3−2 sample. The macropore diameters of the three samples were in the range of 160−210 nm. Changing the organic solvent from EtOH to an EG and MeOH mixture could lead to the Fe_2O_3−7 sample with a high-quality 3DOM structure (Figure 3k,l), similar to that reported by Ueda and co-workers.[18d] Compared to the average diameter (ca. 300 nm) of the hard-template PMMA microspheres, the macropore sizes of these 3DOM Fe_2O_3 materials decreased because of the shrinking of the PMMA microspheres during the calcination processes, and the extent of such shrinking varied greatly depending upon the fabrication conditions adopted. Shown in Figure 4 are the HRTEM images and SAED patterns of the as-fabricated Fe_2O_3−x samples. There was no existence of nanovoids in the walls of the Fe_2O_3−1 sample (Figure 4a). With the introduction of P123, however, the as-fabricated Fe_2O_3−x (x = 2−7) samples showed 3DOM structures with a number of nanovoids (diameter = 2−10 nm) randomly distributed in the walls of macropores (Figure 4d,g,k,m), except for the Fe_2O_3−4 sample, which had been calcined at 650 °C. This result reveals that the surfactant P123 played a crucial role in the generation of nanovoids within the macropore skeletons. In the absence of P123, no nanovoids were formed in the walls of 3DOM Fe_2O_3.[18d] Ueda and co-workers generated 3DOM $LaFeO_3$ with nanovoids on the marcopore walls in the presence of MeOH and EG,[18e] in which EG had an important role to play in the formation of nanovoids on the skeletons of 3DOM $LaFeO_3$. The disappearance of most of the nanovoids in the walls of the 3DOM Fe_2O_3−4 sample might be related to the higher calcination temperature. Additional HRTEM images of 3DOM-architectured Fe_2O_3−x (x = 2, 3, 6, and 7) samples with the presence of nanovoids in the crystalline walls are shown in Figure S3 of the Supporting Information. The results of N_2 adsorption−desorption and pore-size measurements (Figure S4 of the Supporting Information) indicate that there was a copresence of macropores in the majority and nanovoids (mesopores) in the minority of the Fe_2O_3−x (x = 2, 3, and 5−7) samples, but only macropores existed in the Fe_2O_3−1 and Fe_2O_3−4 samples. From the SAED patterns (insets of Figure 4a,c,f,i,k,m,o) of these samples, one can see multiple bright electron diffraction rings, indicating the formation of polycrystalline iron oxide; the recording of a number of noncontinuous bright spots on the SAED patterns of the Fe_2O_3−1 and Fe_2O_3−2 samples implies that the crystallinity of Fe_2O_3−1 and Fe_2O_3−2 obtained after calcination at 550 °C was lower than that of Fe_2O_3−4 obtained after calcination at 650 °C, which was corroborated by the lower XRD signal intensity of the former two samples (Figure 1). The lattice spacing d values of the (104) plane were estimated to be in the range of 0.269−0.270 nm, not far away from that (0.270 nm) of α-Fe_2O_3 (JCPDS no. 87-1164). This result means that the skeletons of the nanovoid-containing 3DOM materials were polycrystalline α-Fe_2O_3. It is worth mentioning that the walls of our 3DOM α-Fe_2O_3 samples were composed of bulk Fe_2O_3 rather than α-Fe_2O_3 nanoparticles, which could be clearly seen from the large-area well-aligned lattice fringes of Figures S3b,h in the Supporting Information. However, the 3DOM walls of the NiO sample reported by Stein and co-workers were composed of numerous NiO nanoparticles, and aggregation of these nanoparticles formed the textural mesopores on the walls of 3DOM NiO.[17h]

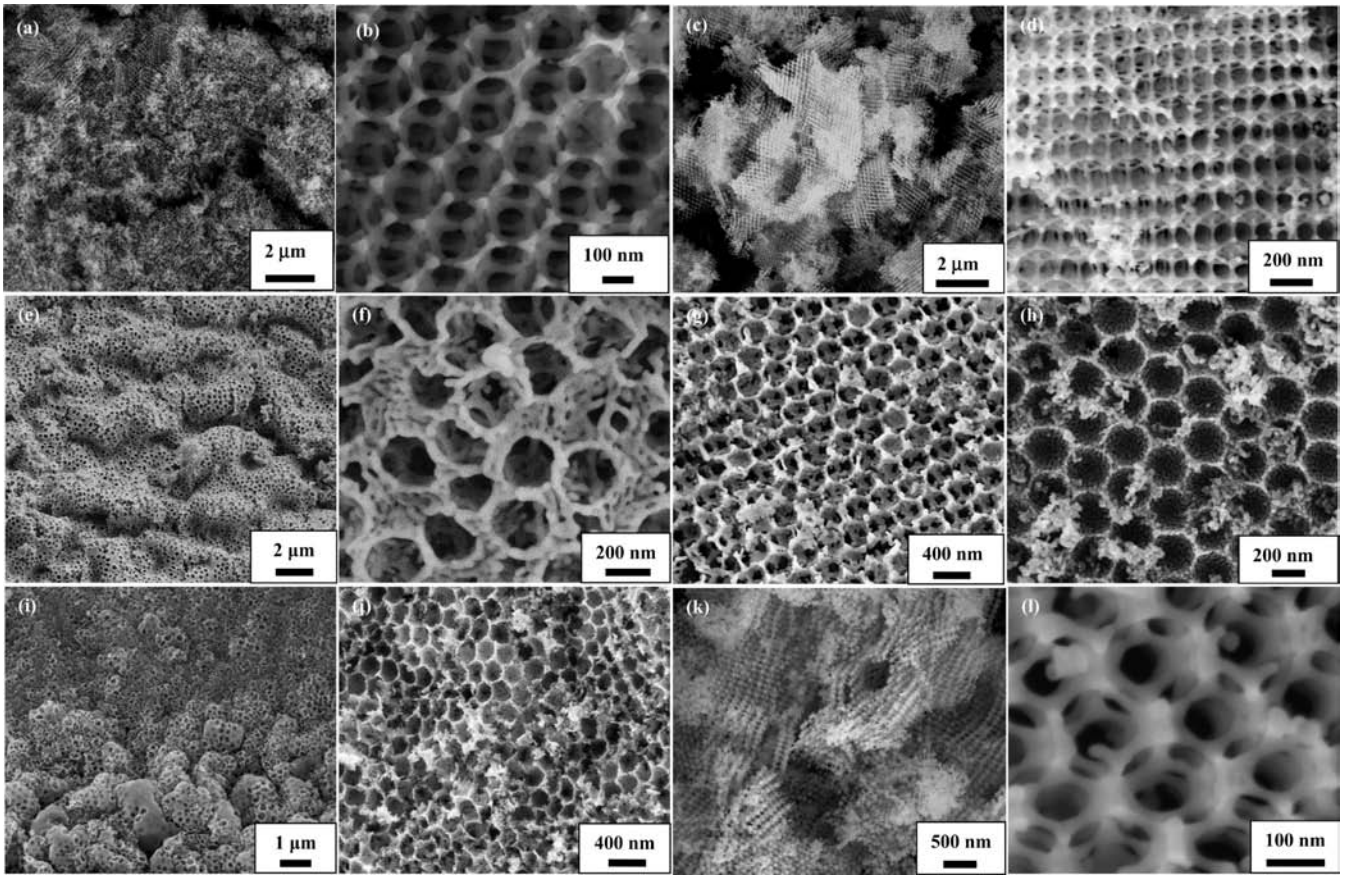

Figure 3. HRSEM images of (a and b) Fe_2O_3−1, (c and d) Fe_2O_3−2, (e and f) Fe_2O_3−3, (g) Fe_2O_3−4, (h) Fe_2O_3−5, (i and j) Fe_2O_3−6, and (k and l) Fe_2O_3−7.

It can be clearly seen from Table 1 that the surface areas (32−46 m^2/g) of the iron oxide samples fabricated with the assistance of P123 and after calcination at 550 °C were significantly higher than those (7−16 m^2/g) of Fe_2O_3−*bulk* and Fe_2O_3−1 fabricated without the assistance of P123. Clearly, the introduction of P123 during the fabrication process was favorable for enhancement of the surface area of the as-fabricated sample, but the amount of P123 added and the nature of the organic solvent seem to have no significant impacts on the surface area in the case of adoption of such a synthesis method. It has been well-known that the calcination temperature exerted a great influence on the surface area of a material. In the present study, a rise in the calcination temperature from 550 to 650 °C induced a marked drop in the surface area from 46.1 m^2/g for Fe_2O_3−3 to 16.9 m^2/g for Fe_2O_3−4, a result plausibly due to the disappearance of most of the nanovoids in the walls of the 3DOM iron oxides. Such a deduction was substantiated by the HRTEM observations of the 3DOM iron oxides. It is worth pointing out that Fe_2O_3−3 calcined at 550 °C exhibited a much higher surface area (ca. 46 m^2/g) than that (ca. 35 m^2/g) of the 3DOM Fe_2O_3 sample after calcination at 500 °C.[18d]

Formation Mechanism. Compared to the average size (ca. 300 nm) of the hard-template PMMA microspheres, the macropore diameter of the as-fabricated iron oxide samples displayed a shrinkage of 33−47%, which was basically consistent with the 26−34% contraction ratio of other macroporous materials (e.g., SiO_2, TiO_2, ZrO_2, and Al_2O_3) obtained by means of similar methods.[29] Although removal of the hard-template PMMA and soft-template P123 via calcination at 550 °C brought about a big contraction in the macropore size, high-quality 3DOM entities were still retained. Figure 5 illustrates the possible formation mechanisms of macroporous iron oxides with and without nanovoid formation in the crystalline walls. In the case of P123-free synthesis, the $Fe(NO_3)_3$ solution infiltrating the voids between the PMMA latex microspheres crystallizes to $Fe(NO_3)_3$ particles after drying; the latter then decomposes to Fe_2O_3 nanoparticles during calcination at 300 °C, and these nanoparticles further agglomerate to form big α-Fe_2O_3 particles until the complete filling of the interstitials between the well-arrayed PMMA microspheres after removal of PMMA during subsequent calcination at 550 °C, thus generating 3DOM-structured α-Fe_2O_3 without the formation of nanovoids in the macroporous walls. In the case of dual-templating (P123 and PMMA) fabrication, however, the above-mentioned mechanism can be used to explain the generation of 3DOM-structured iron oxide. The alcoholic solution containing P123 and ferric nitrate first fills up the interstices of the PMMA latex; the Fe^{3+} ions may undergo complexation with the PEO groups of P123 upon solvent evaporation during the drying process to produce the Fe^{3+}−PEO complexes.[30] The intensity of interactions among PEO−Fe^{3+}−anion species and the molar ratios of Fe/P123 would determine the number and dispersion level of nanovoids within the walls of 3DOM Fe_2O_3. After being dried at ambient temperature and a certain relative humidity, the formed complexes of Fe^{3+} and P123 display a disordered packing within the voids between the PMMA microspheres, thus giving rise to

dx.doi.org/10.1021/ic1023604 |*Inorg. Chem.* 2011, 50, 2534–2544

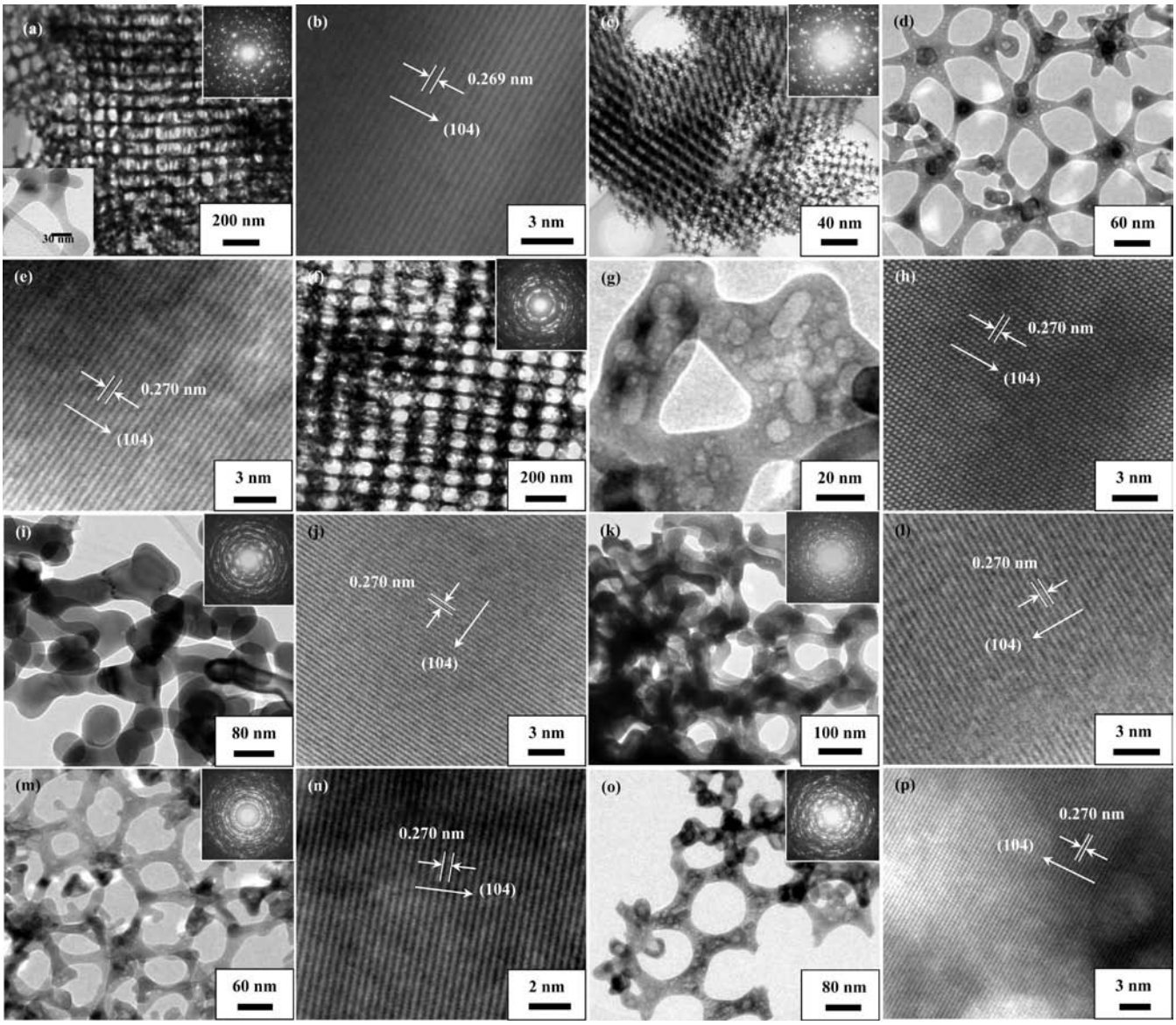

Figure 4. HRTEM images and SAED patterns (insets) of (a and b) Fe_2O_3−1, (c−e) Fe_2O_3−2, (f−h) Fe_2O_3−3, (i and j) Fe_2O_3−4, (k and l) Fe_2O_3−5, (m and n) Fe_2O_3−6, and (o and p) Fe_2O_3−7.

3DOM α-Fe_2O_3 with disordered nanovoids on the macropore walls after oxidative elimination of PMMA and P123 through calcination of the dried sample at 550 °C. Similar formation pathways have been discussed by other researchers.[17h,19b] In addition, with the gradual evaporation of the solvent (EtOH or EG−MeOH) upon drying, the concentration of the surfactant P123 rises to a value higher than the critical micelle concentration,[31] which favors the formation of micelles in a disordered array via interaction of the Fe precursor with the surfactant, hence resulting in the generation of a macropore skeletion with nanovoids. It should be pointed out that the confinement effects of the PMMA latex and interactions of the formed disordered micelles with the polymer microsphere surfaces[19] might also make a contribution to the generation of 3DOM α-Fe_2O_3 with disordered nanovoids on the macropore walls.

Optical Behavior. Iron oxide is one of the most important semiconductor oxides. It possesses four kinds of crystal phases: α-Fe_2O_3 (hematite), γ-Fe_2O_3 (maghemite), Fe_3O_4 (magnetite), and FeO (Wustite).[32] Magnetic Fe_3O_4 and γ-Fe_2O_3 have been utilized in magnetic refrigeration, ferrofluids, controlled drug delivery, bioprocessing, and information storage;[33] α-Fe_2O_3 is a useful material in catalysis, nonlinear optics, gas sensing, and pigment additives.[34] In the past years, iron oxide crystals with rod-, wire-, and core/shell-shaped nanostructures have been successfully fabricated by means of various methods.[35] The physicochemical (especially optical) properties of iron oxide are intimately associated with its morphology and size.[36,37] For example, α-Fe_2O_3 nanoparticles exhibit optical behaviors different from those of mesoporous hollow α-Fe_2O_3 microspheres,[37] α-Fe_2O_3 microcubes,[37] α-Fe_2O_3 nanodisks,[36] and α-Fe_2O_3 nanotubes.[38] Although 3DOM-structured iron oxide was synthesized, its optical property has not been investigated yet. Figure 6 shows the UV−vis diffuse-reflectance spectra of the Fe_2O_3−*bulk* and Fe_2O_3−*x* (*x* = 1−7) samples. It is observed that there are signals centered at ca. 240, 340, 434, 540, and 670 nm,

dx.doi.org/10.1021/ic1023604 |*Inorg. Chem.* 2011, 50, 2534–2544

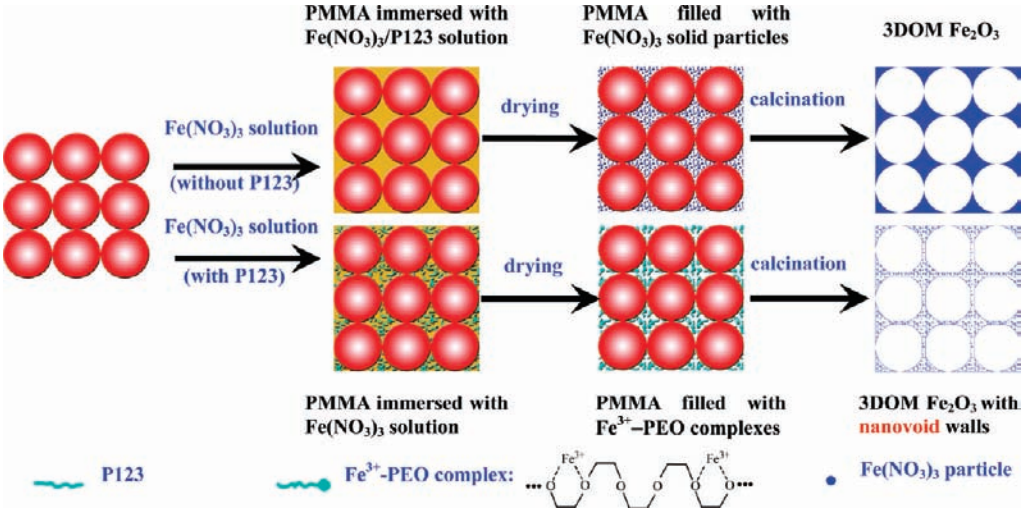

Figure 5. Schematic illustration of possible formation mechanisms of the macroporous α-Fe_2O_3 samples with and without the presence of nanovoids in the crystalline walls.

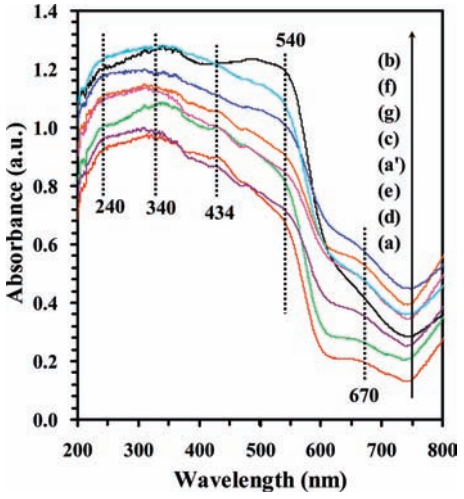

Figure 6. UV−vis spectra of (a′) Fe_2O_3−*bulk*, (a) Fe_2O_3−1, (b) Fe_2O_3−2, (c) Fe_2O_3−3, (d) Fe_2O_3−4, (e) Fe_2O_3−5, (f) Fe_2O_3−6, and (g) Fe_2O_3−7.

characteristic of α- Fe_2O_3. The absorption bands in the region of 200−440 nm are mainly due to the ligand-to-metal charge-transfer transitions and partly due to the Fe^{3+} ligand-field transitions $^6A_1 \rightarrow {}^4T_1$ (^4P) at ca. 240 nm, $^6A_1 \rightarrow {}^4E$ (^4D) and $^6A_1 \rightarrow {}^4T_2$ (^4D) at 340 nm, and $^6A_1 \rightarrow {}^4E$ (^4G) at 434 nm.[39a,b] Absorption bands near 540 and 670 nm correspond to $^6A_1 \rightarrow {}^4E$ and $^6A_1 \rightarrow {}^4T_2$ (^4G) ligand-field transitions of Fe^{3+}.[39c] The absorbance is different from sample to sample, which was associated with their crystallinity and pore structures.[37] Band-gap energy is usually used to evaluate the optical absorption performance of a crystal semiconductor, which is based on the Kubelka−Munk (K−M) function $F(R) = (1 - R)^2/2R = K/S$, where R, K, and S represent the reflectance, absorption coefficient, and scattering coefficient, respectively. The band-gap energies of the iron oxide samples can be obtained from the intercept of the tangent to the x axis in the plot of $F(R)$ versus photon energy (Figure S5 in the Supporting Information), and the results are summarized in Table 1. It is observed that the nonporous Fe_2O_3−*bulk* and 3DOM-structured Fe_2O_3−1 and Fe_2O_3−4 (without nanovoids in the walls) samples exhibit much higher band-gap energies (2.06−2.10 eV) than those (1.92−2.03 eV) of the 3DOM-structured Fe_2O_3−x (x = 2, 3, and 5−7) samples with nanovoids in the macroporous walls, with the Fe_2O_3−3 sample possessing the lowest band-gap energy (1.92 eV), which was much lower than that (2.1 eV) of α-Fe_2O_3 nanodisks[36] or α-Fe_2O_3 nanoparticles[39c] and that (2.18 eV) of α-Fe_2O_3 nanotubes.[38] The band-gap energy of a material usually increases with a decrease in the particle size. In one of our previous works, we observed that the band-gap energy changed with alteration of the particle morphology of monoclinic $BiVO_4$.[22] In the present work, a similar change trend in the band-gap energy was observed. Such a phenomenon might be due to the presence of macropores and nanovoids on the walls of the 3DOM iron oxides. These macropores and nanovoids could lead to a drop in the reflection intensity of incident light, resulting in a decrease in the value of the K−M function [$F(R)$] and, hence, the $F(R)$ value increased slowly with a rise in the photon energy. Therefore, it is understandable that the samples with macropores and nanovoids on the 3DOM Fe_2O_3 skeletons showed lower band-gap energies. Ueda and co-workers also observed an optical behavior of 3DOM $LaFeO_3$ with nanovoids different from that of the nonporous $LaFeO_3$,[18e] although they did not give a discussion on the discrepancy in the optical behavior between the 3DOM $LaFeO_3$ with nanovoids and nonporous $LaFeO_3$. The inherent reason for the unusual phenomenon occurrence needs further investigation.

Surface Composition and Reducibility. The XPS technique is a powerful tool to investigate the surface element compositions, metal chemical valence, and adsorbed species of solid materials. As can be seen from the Fe 2p XPS spectra of the iron oxide samples (Figure S6 in the Supporting Information), there are two strong signals centered at BE = 710.8 and 724.4 eV assignable to Fe $2p_{3/2}$ and Fe $2p_{1/2}$,[40] respectively; meanwhile, one weak satellite signal at BE = 718.0 eV was detected for each sample, indicating the presence of a small amount of Fe^{2+}.[40] Similar XPS spectra of α-Fe_2O_3 have been reported by other authors.[41,42] Figure 7 illustrates the Fe $2p_{3/2}$ and O 1s XPS spectra of the Fe_2O_3−*bulk* and Fe_2O_3−x samples. The asymmetrical Fe $2p_{3/2}$ XPS peak of each sample could be decomposed to two components at BE = 710.3

dx.doi.org/10.1021/ic1023604 |*Inorg. Chem.* 2011, 50, 2534–2544

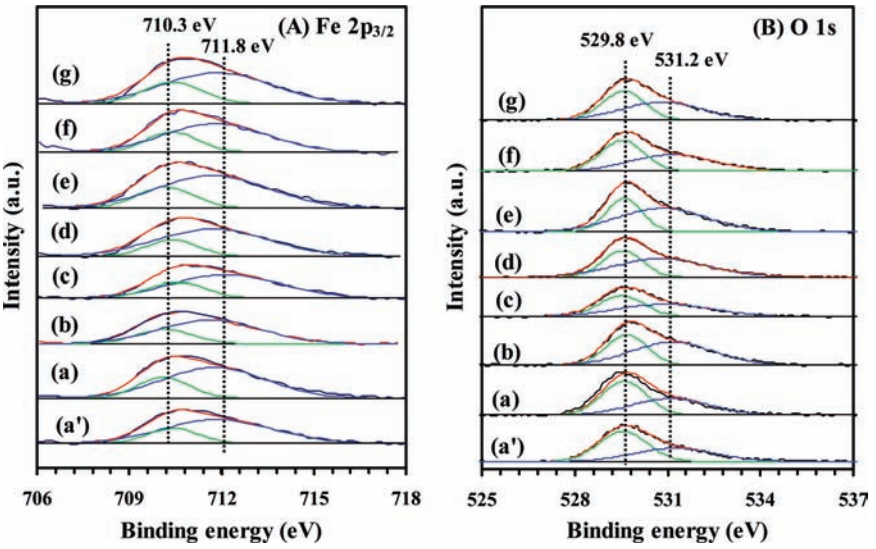

Figure 7. (A) Fe $2p_{3/2}$ and (B) O 1s XPS spectra of (a′) Fe_2O_3−*bulk*, (a) Fe_2O_3−1, (b) Fe_2O_3−2, (c) Fe_2O_3−3, (d) Fe_2O_3−4, (e) Fe_2O_3−5, (f) Fe_2O_3−6, and (g) Fe_2O_3−7.

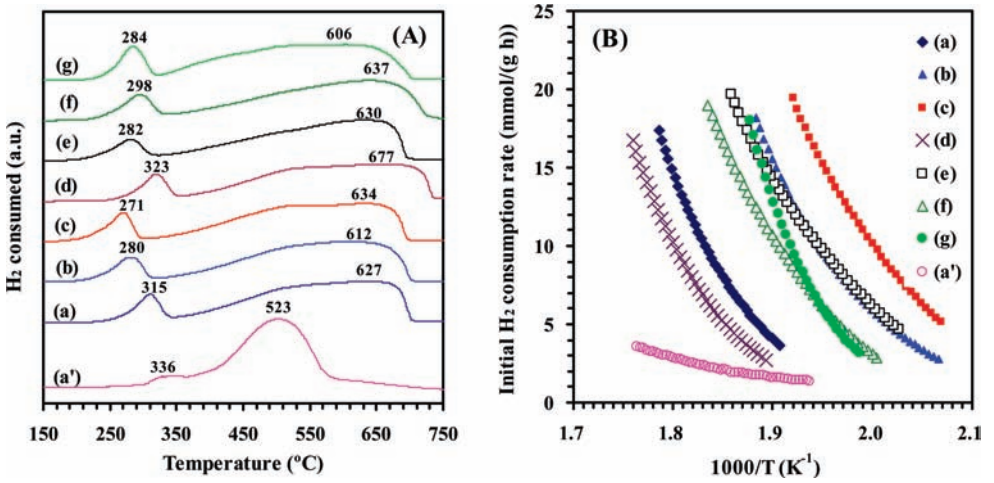

Figure 8. (A) H_2-TPR profiles and (B) the initial H_2 consumption rate as a function of the inverse temperature of (a′) Fe_2O_3−*bulk*, (a) Fe_2O_3−1, (b) Fe_2O_3−2, (c) Fe_2O_3−3, (d) Fe_2O_3−4, (e) Fe_2O_3−5, (f) Fe_2O_3−6, and (g) Fe_2O_3−7.

and 711.8 eV (Figure 7A), ascribable to the Fe^{2+} and Fe^{3+} signals,[42−44] respectively. Table 1 summarizes the surface iron and oxygen compositions of the samples. It is observed that the Fe^{3+}/Fe^{2+} molar ratios (3.59−3.61) of Fe_2O_3−*bulk* and Fe_2O_3−4 after calcination at 650 °C were much higher than those (2.75−3.08) of Fe_2O_3−x (x = 1−3 and 5−7) after calcination at 550 °C. This result suggests that a higher calcination temperature favors the formation of Fe^{3+} ions. From Figure 7B, one can see an asymmetrical O 1s XPS peak of each sample that could be resolved into two components at BE = 529.8 and 531.2 eV; the former was attributable to the surface lattice oxygen (O_{latt}) species and the latter to the surface-adsorbed oxygen (O_{ads}) species.[44,45] The O_{ads}/O_{latt} molar ratios (0.74−0.87) of Fe_2O_3−*bulk*, Fe_2O_3−1, and Fe_2O_3−4 were significantly lower than those (1.04−1.63) of Fe_2O_3−x (x = 2, 3, and 5−7), indicating that the Fe_2O_3 samples possessed much larger amounts of oxygen adspecies than the ones with lower surface areas.

Reducibility of a transition-metal oxide is highly related to its catalytic performance. Usually, the reduction of iron oxide proceeds via the order of α-Fe_2O_3 → Fe_3O_4 → Fe^0.[43,46] Figure 8A illustrates the H_2-TPR profiles of the as-fabricated iron oxide samples. For each sample, two reduction steps were clearly observed in the ranges of 190−350 and 350−700 °C, corresponding to the reduction of α-Fe_2O_3 to Fe_3O_4[47] and the reduction of Fe_3O_4 to Fe^0.[43,47] The H_2 consumption of each sample was estimated and summarized in Table 1. For the Fe_2O_3−*bulk* and Fe_2O_3−x (x = 1−7) samples, the H_2 consumption values at the lower reduction temperature (190−350 °C) were 1.05 and 1.91−2.46 mmol/g, whereas that at the higher reduction temperature (350−700 °C), they were 16.1 and 12.8−13.7 mmol/g, respectively. If the Fe ions in α-Fe_2O_3 were only Fe^{3+} and Fe^{2+} and reduced to metallic Fe^0, the H_2 consumption would be 18.74 and 13.89 mmol/g, accordingly. As revealed in the H_2-TPR results, the H_2 consumption in the range of 190−700 °C of the Fe_2O_3−*bulk* and Fe_2O_3−x samples was between 14.81 and 17.15 mmol/g. It is apparent that the Fe ions in our α-Fe_2O_3 samples existed in a mixed valence (Fe^{3+} and Fe^{2+}), which was substantiated by the results of XPS investigations.

dx.doi.org/10.1021/ic1023604 |*Inorg. Chem.* 2011, 50, 2534–2544

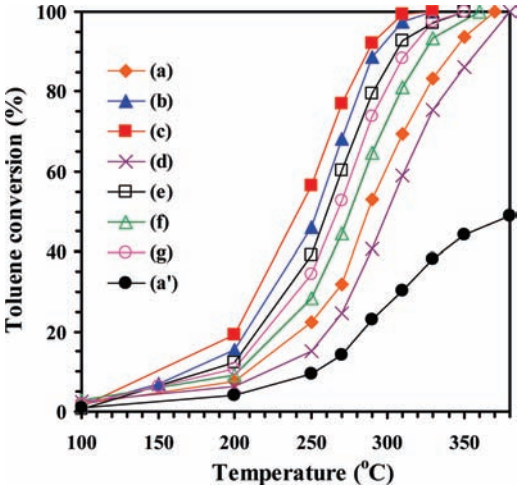

Figure 9. Catalytic performance as a function of the reaction temperature over (a′) Fe_2O_3−*bulk*, (a) Fe_2O_3−1, (b) Fe_2O_3−2, (c) Fe_2O_3−3, (d) Fe_2O_3−4, (e) Fe_2O_3−5, (f) Fe_2O_3−6, and (g) Fe_2O_3−7 under the conditions of toluene concentration = 1000 ppm, toluene/oxygen molar ratio = 1/20, and SV = 20 000 mL/(g h).

The initial (where less than 25% oxygen in iron oxide was consumed for the first reduction band) H_2 consumption rate is more effective in evaluating the reducibility of the samples.[48] Figure 8B shows the initial H_2 consumption rate versus inverse temperature of the as-fabricated iron oxide samples. One can realize that the initial H_2 consumption rate followed a sequence of Fe_2O_3−3 > Fe_2O_3−2 ≈ Fe_2O_3−5 > Fe_2O_3−7 > Fe_2O_3−6 > Fe_2O_3−1 > Fe_2O_3−4 > Fe_2O_3−*bulk*, in rough agreement with the order in the surface area of these materials.

Catalytic Property. Transition-metal oxides are a kind of effective catalysts. In the past years, Fe-based materials [e.g., iron(III) oxide pillared titanium phosphate[49] and Fe_2O_3[50,51]] have been employed as catalysts for the removal of volatile organic compounds (e.g., methanol, acetone, diethyl ether, 2-propanol, and toluene), and the good catalytic performance was attributed to the presence of high surface area and surface oxygen concentration.[49] Scirè and co-workers observed a toluene conversion of 90% over the Fe_2O_3 catalyst at ca. 380 °C and a rather low space velocity (SV) of ca. 186 mL/(g h).[51] Durán et al. reported that 80% toluene conversion could be achieved over Fe_2O_3 at 365 °C and 20 000 mL/(g h).[52] In the present work, we used toluene oxidation as a model reaction to evaluate the catalytic properties of the as-fabricated iron oxide samples. In the blank experiment (only quartz sand was loaded in the microreactor), we detected no significant oxidation of toluene under the conditions of toluene concentration = 1000 ppm, toluene/O_2 molar ratio = 1/20, SV = 20 000 mL/(g h), and reaction temperature ≤ 400 °C. In other words, oxidation of the toluene molecules over the iron oxide samples was a catalytic process. Figure 9 shows the catalytic performance of the Fe_2O_3−*bulk* and Fe_2O_3−*x* samples for toluene combustion. It can be clearly observed that toluene conversion increased with a rise in the reaction temperature, and Fe_2O_3−*x* performed much better than *bulk*-Fe. It is convenient to compare the catalytic activities of these samples by adopting the reaction temperatures $T_{10\%}$, $T_{50\%}$, and $T_{90\%}$ (corresponding to toluene conversion = 10, 50, and 90%), and the corresponding data are summarized in Table S1 in the Supporting Information. Apparently, the catalytic performance decreased in the sequence of Fe_2O_3−3 > Fe_2O_3−2 > Fe_2O_3−5 > Fe_2O_3−7 > Fe_2O_3−6 > Fe_2O_3−1 > Fe_2O_3−4 > Fe_2O_3−*bulk*, coinciding with the order in low-temperature reducibility (i.e., the initial H_2 consumption rate) of these materials. The $T_{50\%}$ and $T_{90\%}$ values were 240 and 288 °C over the Fe_2O_3−3 sample and 253 and 293 °C over the Fe_2O_3−2 sample, whereas over the Fe_2O_3−*bulk* sample, they were above 380 °C. Obviously, the catalytic activities of the 3DOM iron oxide samples were much better than those of Fe_2O_3 reported by other researchers.[51,52] It is worth pointing out that toluene was completely oxidized to CO_2 and H_2O over the as-fabricated iron oxide samples; no other incomplete oxidation products were detected in the catalytic system, which was confirmed by the carbon balance of ca. 99.5% in each run.

It is generally accepted that the surface oxygen concentration, reducibility, surface area, and pore structure are the key factors influencing the catalytic performance of a single or mixed transition-metal oxide. By a comparison of the activity data and characterization results obtained in our present studies, it can be realized that there is a clear relationship of the BET surface area (Table 1), adsorbed oxygen concentration (Figure 7B and Table 1), low-temperature reducibility (Figure 8), or band-gap energy (Figure S5 in the Supporting Information and Table 1) with the catalytic activity (Figure 9 and Table S1 in the Supporting Information). Therefore, we conclude that the excellent catalytic performance of the 3DOM-structured Fe_2O_3 samples is associated with their higher surface areas and concentrations of surface oxygen species, better low-temperature reducibility, and unique nanovoid-containing 3DOM structures.

CONCLUSIONS

3DOM-organized iron oxides with the existence of nanovoids in the rhombohedral crystalline walls could be fabricated via the dual-templating P123 and PMMA route with $Fe(NO_3)_3$ as the iron source in an EtOH or EG−MeOH mixed solution and after calcination at 550 °C. In the absence of P123 during the fabrication process, only 3DOM-structured α-Fe_2O_3 without nanovoids in the macropore walls was obtained; with the use of dual (P123 and PMMA) templates, however, high-quality 3DOM-organized α-Fe_2O_3 materials with polycrystalline nanovoid-containing walls and higher surface areas (32−46 m^2/g) were generated. The surfactant P123 had a key role to play in the formation of nanovoids within the walls of the 3DOM-structured α-Fe_2O_3. Iron existed in multiple oxidation states on the sample surfaces, and the trivalent Fe ion and oxygen adspecies amounts were different from sample to sample, respectively. The dual-templating-derived α-Fe_2O_3 samples possessed much better low-temperature reducibility than the Fe_2O_3−*bulk* one. The discrepancy in the pore structure gave rise to a different optical behavior, and the copresence of a 3DOM-structured skeleton and a nanovoid-containing wall structure led to a decrease in the band-gap energy of α-Fe_2O_3. Factors, such as a higher oxygen adspecies amount, larger surface area, better low-temperature reducibility, and unique nanovoid-containing 3DOM structure, contributed to the excellent catalytic activities of the porous materials in the oxidation of toluene.

ASSOCIATED CONTENT

Supporting Information. Physicochemical property characterization procedures, the SEM image of well-aligned PMMA microspheres, FT-IR spectra of uncalcined Fe_2O_3−2, calcined

Fe_2O_3−2, uncalcined Fe_2O_3−6, and calcined Fe_2O_3−6, additional HRTEM images of Fe_2O_3−x (x = 2, 3, 6, and 7), N_2 adsorption−desorption isotherms and pore-size distributions, K−M function versus photon energy of the Fe_2O_3−*bulk* and Fe_2O_3−x (x = 1−7), Fe 2p XPS spectra of Fe_2O_3−*bulk* and Fe_2O_3−x (x = 1−7), and catalytic data ($T_{10\%}$, $T_{50\%}$, and $T_{90\%}$) of Fe_2O_3−*bulk* and Fe_2O_3−x (x = 1−7). This material is available free of charge via the Internet at http://pubs.acs.org.

AUTHOR INFORMATION

Corresponding Author

*E-mail: hxdai@bjut.edu.cn. Tel.: +86-10-6739-6118. Fax: +86-10-6739-1983.

ACKNOWLEDGMENT

The work described above was supported by the projects granted by the National Natural Science Foundation of China (Grants 20973017 and 21077007), the Creative Research Foundation of Beijing University Technology (Grant 00500054R4003), the Natural Science Foundation of Beijing Municipality (Grant 2102008), the "863" Key Program of Ministry of Science and Technology of China (Grant 2009AA063201), and the Creative Research Team of Beijing Municipal Commission of Education (Grants PHR200907105 and PHR201007105). We also thank Jianping He (State Key Laboratory of Advanced Metals and Materials, University of Science & Technology Beijing) for doing the HRSEM analyses of the samples.

REFERENCES

(1) (a) Antonelli, D. M.; Ying, Y. J. *Chem. Mater.* **1996**, *8*, 874. (b) Corma, A. *Chem. Rev.* **1997**, *97*, 2373. (c) Braun, P. V.; Osenar, P.; Tohvev, V.; Kennedy, S. B.; Stupp, S. I. *J. Am. Chem. Soc.* **1999**, *121*, 7302. (d) Barton, T. J.; Bull, L. M.; Klemperer, M. G.; Loy, D. A.; Mcenaney, B.; Misono, M.; Monson, P. A.; Pez, G.; Scherer, G. W.; Vartuli, J. C.; Yaghi, O. M. *Chem. Mater.* **1999**, *11*, 2633. (e) Jaroniec, M.; Kruk, M.; Shin, H. J.; Ryoo, R.; Sakamoto, Y.; Terasaki, O. *Microporous Mesoporous Mater.* **2001**, *48*, 127. (f) Sayari, A.; Hamoudi, S. *Chem. Mater.* **2001**, *13*, 3151.

(2) Perkas, N.; Palchik, O.; Brukental, I.; Nowik, I.; Gofer, Y.; Koltypin, Y.; Gedanken, A. *J. Phys. Chem. B* **2003**, *107*, 8772.

(3) Liu, Q.; Zhang, W.-M.; Cui, Z.-M.; Zhang, B.; Wan, L.-J.; Song, W.-G. *Microporous Mesoporous Mater.* **2007**, *100*, 233.

(4) Srivastava, D. N.; Perkas, N.; Gedanken, A.; Felner, I. *J. Phys. Chem. B* **2002**, *106*, 1878.

(5) Wan, L. J.; Shi, K. Y.; Tian, X. Q.; Fu, H. G. *J. Solid State Chem.* **2008**, *181*, 735.

(6) Brezesinski, T.; Groenewolt, M.; Antonietti, M.; Smarsly, B. *Angew. Chem., Int. Ed.* **2006**, *45*, 781.

(7) Wang, Y.; Yin, L.; Gedanken, A. *Ultrason. Sonochem.* **2002**, *9*, 285.

(8) Shi, K. Y.; Peng, L.-M.; Chen, Q.; Wang, R. H.; Zhou, W. Z. *Microporous Mesoporous Mater.* **2005**, *83*, 219.

(9) Jiao, F.; Harrison, A.; Jumas, J.-C.; Chadwick, A. V.; Kockelmann, W.; Bruce, P. G. *J. Am. Chem. Soc.* **2006**, *128*, 5468.

(10) Jiao, F.; Bruce, P. G. *Angew. Chem., Int. Ed.* **2004**, *43*, 5958.

(11) Kang, M.; Kim, D.; Yi, S. H.; Han, J. U.; Yie, J. E.; Kim, J. M. *Catal. Today* **2004**, *93*−*95*, 695.

(12) Kong, A. G.; Wang, H. W.; Li, J.; Shan, Y. K. *Mater. Lett.* **2008**, *62*, 943.

(13) Han, L.; Shan, Z.; Chen, D. H.; Yu, X. J.; Yang, P. Y.; Tu, B.; Zhao, D. Y. *J. Colloid Interface Sci.* **2008**, *318*, 315.

(14) Lezau, A.; Trudeau, M.; Tsoi, G. M.; Wenger, L. E.; Antonelli, D. *J. Phys. Chem. B* **2004**, *108*, 5211.

(15) Yu, C. H.; Dong, X. P.; Guo, L. M.; Li, J. T.; Qin, F.; Zhang, L. X.; Shi, J. L.; Yan, D. S. *J. Phys. Chem. C* **2008**, *112*, 13378.

(16) Zhou, W. J.; He, W.; Zhong, S. D.; Wang, Y. J.; Zhao, H. S.; Li, Z. M.; Yan, S. P. *J. Magn. Magn. Mater.* **2009**, *321*, 1025.

(17) (a) Stein, A.; Schroden, R. C. *Curr. Opin. Solid State Mater. Sci.* **2001**, *5*, 553. (b) Stein, A. *Microporous Mesoporous Mater.* **2001**, *44*−*45*, 227.(c) Schroden, R. C.; Stein, A. In *3D Ordered Macroporous Material, Colloids and Colloid Assemblies*; Caruso, F., Ed.; Wiley-VCH Verlag GmbH and Co. KGaA: Weinheim, Germany, 2004; p 465. (d) Srinivasan, M.; White, T. *Environ. Sci. Technol.* **2007**, *41*, 4405. (e) Tonti, D.; Torralvo, M. J.; Enciso, E.; Sobrados, I.; Sanz, J. *Chem. Mater.* **2008**, *20*, 4783. (f) Sorensen, E. M.; Barry, S. J.; Jung, H.-K.; Rondinelli, J. M.; Vaughey, J. T.; Poeppelmeier, K. R. *Chem. Mater.* **2006**, *18*, 482. (g) Blanford, C. F.; Carter, C. B.; Stein, A. *J. Mater. Sci.* **2008**, *43*, 3539. (h) Yan, H.; Blanford, C. F.; Holland, B. T.; Smyrl, W. H.; Stein, A. *Chem. Mater.* **2000**, *12*, 1134.

(18) (a) Sadakane, M.; Asanuma, T.; Kubo, J.; Ueda, W. *Chem. Mater.* **2005**, *17*, 3546. (b) Sadakane, M.; Takahashi, C.; Kato, N.; Asanuma, T.; Ogihara, H.; Ueda, W. *Chem. Lett.* **2006**, *35*, 480. (c) Sadakane, M.; Takahashi, C.; Kato, N.; Ogihara, H.; Nodasaka, Y.; Doi, Y.; Hinatsu, Y.; Ueda, W. *Bull. Chem. Soc. Jpn.* **2007**, *80*, 677. (d) Sadakane, M.; Horiuchi, T.; Kato, N.; Takahashi, C.; Ueda, W. *Chem. Mater.* **2007**, *19*, 5779. (e) Sadakane, M.; Horiuchi, T.; Kato, N.; Sasaki, K.; Ueda, W. *J. Solid State Chem.* **2010**, *183*, 1365.

(19) (a) Yang, P.; Deng, T.; Zhao, D.; Feng, P.; Pine, D.; Chmelka, B. F.; Whitesides, G. M.; Stucky, G. D. *Science* **1998**, *282*, 2244. (b) Luo, Q.; Li, L.; Yang, B.; Zhao, D. *Chem. Lett.* **2000**, *29*, 378. (c) Yang, Z.; Qi, K.; Rong, J.; Wang, L.; Liu, Z.; Yang, Y. *Chin. Sci. Bull.* **2001**, *46*, 1349. (d) Li, F.; Wang, Z.; Ergang, N. S.; Fyfe, C. A.; Stein, A. *Langmuir* **2007**, *23*, 3996.

(20) Holland, B. T.; Abrams, L.; Stein, A. *J. Am. Chem. Soc.* **1999**, *121*, 4308.

(21) (a) Niu, J. R.; Deng, J. G.; Liu, W.; Zhang, L.; Wang, G. Z.; Dai, H. X.; He, H.; Zi, X. H. *Catal. Today* **2007**, *126*, 420. (b) Deng, J. G.; Zhang, L.; Dai, H. X.; He, H.; Au, C. T. *Ind. Eng. Chem. Res.* **2008**, *47*, 8175. (c) Deng, J. G.; Zhang, Y.; Dai, H. X.; Zhang, L.; He, H.; Au, C. T. *Catal. Today* **2008**, *139*, 82. (d) Deng, J. G.; Dai, H. X.; Jiang, H. Y.; Zhang, L.; Wang, G. Z.; He, H.; Au, C. T. *Environ. Sci. Technol.* **2010**, *44*, 2618. (e) Deng, J. G.; Zhang, L.; Dai, H. X.; Au, C. T. *Appl. Catal., A* **2009**, *352*, 43.

(22) Meng, X.; Zhang, L.; Dai, H. X.; Zhao, Z. X.; Zhang, R. Z.; Liu, Y. X. *Mater. Chem. Phys.* **2011**, *125*, 59.

(23) Wang, G. Z.; Zhang, L.; Dai, H. X.; Deng, J. G.; Liu, C. X.; He, H.; Au, C. T. *Inorg. Chem.* **2008**, *47*, 4015.

(24) Liu, C. X.; Zhang, L.; Deng, J. G.; Mu, Q.; Dai, H. X.; He, H. *J. Phys. Chem. C* **2008**, *112*, 19248.

(25) Li, H. N.; Zhang, L.; Dai, H. X.; He, H. *Inorg. Chem.* **2009**, *48*, 4421.

(26) (a) Xia, Y. S.; Dai, H. X.; Jiang, H. Y.; Deng, J. G.; He, H.; Au, C. T. *Environ. Sci. Technol.* **2009**, *43*, 8355. (b) Deng, J. G.; Zhang, L.; Dai, H. X.; Xia, Y. S.; Jiang, H. Y.; Zhang, H.; He, H. *J. Phys. Chem. C* **2010**, *114*, 2694.

(27) (a) Raming, T. P.; Winnubst, A. J. A.; Kats, C. M.; Philipse, P. A. *J. Colloid Interface Sci.* **2002**, *249*, 346. (b) Sarangi, P. P.; Naik, B.; Ghosh, N. N. *Powder Technol.* **2009**, *192*, 245.

(28) Gabelica, Z.; Charmot, A.; Vataj, R.; Soulimane, R.; Barrault, J.; Valange, S. *J. Therm. Anal. Calorim.* **2009**, *95*, 445.

(29) (a) Holland, B. T.; Blanford, C. F.; Do, T.; Stein, A. *Chem. Mater.* **1999**, *11*, 795. (b) Holland, B. T.; Blanford, C. F.; Stein, A. *Science* **1998**, *281*, 538.

(30) (a) Wang, Y. G.; Ren, J. W.; Liu, X. H.; Wang, Y. Q.; Guo, Y.; Guo, Y. L.; Lu, G. Z. *J. Colloid Interface Sci.* **2008**, *326*, 158. (b) Wang, Y. M.; Wu, Z. Y.; Wei, Y. L.; Zhu, J. H. *Microporous Mesoporous Mater.* **2005**, *84*, 127.

(31) Lu, Y.; Gangull, R.; Drewien, C. A.; Anderson, M. T.; Brinker, C. J.; Gong, W.; Huang, M. H.; Zink, J. I. *Nature (London)* **1997**, *389*, 364.

(32) Sahu, P.; De, M.; Zdujić, M. *Mater. Chem. Phys.* **2003**, *82*, 864.

(33) (a) Hyeon, T. *Chem. Commun.* **2003**, 927. (b) Wang, J.; Chen, Q.; Zeng, C.; Hou, B. *Adv. Mater.* **2004**, *16*, 137.
(34) (a) Dong, W.; Zhu, C. *J. Mater. Chem.* **2002**, *12*, 1676. (b) Li, P.; Miser, D. E.; Rabiei, S.; Yadav, R. T.; Hajaligol, M. R. *Appl. Catal., B* **2003**, *43*, 151.
(35) (a) Bourlinos, A. B.; Simopoulos, A.; Petridis, D. *Chem. Mater.* **2002**, *14*, 899. (b) Woo, K.; Lee, H. J.; Ahn, J.-P.; Park, Y. S. *Adv. Mater.* **2003**, *15*, 1761. (c) Zeng, H.; Li, J.; Wang, Z. L.; Liu, J. P.; Sun, S. *Nano Lett.* **2004**, *4*, 187.
(36) Chen, D. L.; Gao, L. *Chem. Phys. Lett.* **2004**, *395*, 316.
(37) Lian, J. B.; Duan, X. C.; Ma, J. M.; Peng, P.; Kim, T.; Zheng, W. J. *ACS Nano* **2009**, *3*, 3749.
(38) Zhang, Z. H.; Hossain, Md. F.; Takahashi, T. *Appl. Catal., B* **2010**, *3*−*4*, 423.
(39) (a) Sherman, D. M.; Waite, T. D. *Am. Mineral.* **1985**, *70*, 1262. (b) Hashimoto, T.; Yamada, T.; Yoko, T. *J. Appl. Phys.* **1996**, *80*, 3184. (c) Kleiman-Shwarsctein, A.; Hu, Y.-S.; Forman, A. J.; Stucky, G. D.; McFarland, E. W. *J. Phys. Chem. C* **2008**, *112*, 15900.
(40) Moulder, J. F.; Stickle, W. F.; Sobol, P. E.; Bomben, K. D. *Handbook of X-ray Photoelectron Spectroscopy*; Perkin-Elmer Co.: Waltham, MA, 1992.
(41) Muhler, M.; Schlögl, R.; Eder, S.; Ertl, G. *Surf. Sci.* **1987**, *189*−*190*, 69.
(42) Brundle, C. R.; Chuang, T. J.; Wandelt, K. *Surf. Sci.* **1977**, *68*, 459.
(43) Castro, C. S.; Olievira, L. C. A.; Guerreiro, M. C. *Catal. Lett.* **2009**, *133*, 41.
(44) (a) Ismail, H. M.; Cadenhead, D. A.; Zaki, M. I. *J. Colloid Interface Sci.* **1997**, *194*, 482. (b) Yamashita, T.; Hayes, P. *Appl. Surf. Sci.* **2008**, *254*, 2441.
(45) (a) Allen, G. C.; Curtis, M. T.; Hooper, A. J.; Tucker, P. M. *J. Chem. Soc., Dalton Trans.* **1974**, 1525. (b) Cao, W.; Tan, O. K.; Pan, J. S.; Zhu, W.; Gopal Reddy, C. V. *Mater. Chem. Phys.* **2002**, *75*, 67. (c) Dupin, J. C.; Gonbeau, D.; Vinatier, P.; Levasseur, A. *Phys. Chem. Chem. Phys.* **2000**, *2*, 1319.
(46) Unmuth, E. E.; Schwarta, L. H.; Butt, J. B. *J. Catal.* **1980**, *61*, 242.
(47) (a) Rombi, E.; Ferino, I.; Monaci, R.; Picciau, C.; Solinas, V.; Buzzoni, R. *Appl. Catal., A* **2004**, *266*, 73. (b) Yang, Q.; Choi, H.; Al-Abed, S. R.; Dionysiou, D. D. *Appl. Catal., B* **2009**, *88*, 462.
(48) Dai, H. X.; Bell, A. T.; Iglesia, E. *J. Catal.* **2004**, *221*, 491.
(49) Das, D. P.; Parida, K. M. *J. Mol. Catal., A* **2007**, *276*, 17.
(50) Morales, M. R.; Barbero, B. P.; Cadús, L. E. *Appl. Catal., B* **2007**, *74*, 1.
(51) (a) Minicò, S.; Scirè, S.; Crisafulli, C.; Maggiore, R.; Galvagno, S. *Appl. Catal., B* **2000**, *28*, 245. (b) Scirè, S.; Minicò, S.; Crisafulli, C.; Galvagno, S. *Catal. Commun.* **2001**, *2*, 229. (c) Minicò, S.; Scirè, S.; Crisafulli, C.; Galvagno, S. *Appl. Catal., B* **2001**, *34*, 277.
(52) Durán, F. G.; Barbero, B. P.; Cadús, L. E.; Rojas, C.; Centeno, M. A.; Odriozola, J. A. *Appl. Catal., B* **2009**, *92*, 194.